Experimental and Computational Exploration of the NaF-ThF_4 Fuel System Structure and Thermochemistry

Schreuder, Maarten B.J.W.; Ocádiz Flores, Jaén A.; Gheribi, Aimen E.; Beneš, Ondrej; Griveau, Jean Christophe; Colineau, Eric; Konings, Rudy J.M.; Smith, Anna Louise

DOI
10.1021/acs.jpcb.1c04830

Publication date
2021

Document Version
Final published version

Published in
Journal of Physical Chemistry B

THE JOURNAL OF PHYSICAL CHEMISTRY B
A JOURNAL OF THE AMERICAN CHEMICAL SOCIETY

pubs.acs.org/JPCB

Article

Experimental and Computational Exploration of the NaF−ThF_4 Fuel System: Structure and Thermochemistry

Maarten B. J. W. Schreuder, Jaén A. Ocádiz Flores, Aimen E. Gheribi, Ondrej Beneš, Jean-Christophe Griveau, Eric Colineau, Rudy J. M. Konings, and Anna Louise Smith*

Cite This: *J. Phys. Chem. B* 2021, 125, 8558−8571

Read Online

ACCESS | Metrics & More | Article Recommendations | Supporting Information

ABSTRACT: The structural, thermochemical, and thermophysical properties of the NaF−ThF_4 fuel system were studied with experimental methods and molecular dynamics (MD) simulations. Equilibrium MD (EMD) simulations using the polarizable ion model were performed to calculate the density, molar volume, thermal expansion, mixing enthalpy, heat capacity, and distribution of $[ThF_n]^{m-}$ complexes in the $(Na,Th)F_x$ melt over the full concentration range at various temperatures. The phase equilibria in the 10−50 mol % ThF_4 and 85−95 mol % ThF_4 regions of the NaF−ThF_4 phase diagram were measured using differential scanning calorimetry, as were the mixing enthalpies at 1266 K of (NaF/ThF_4) = (0.8:0.2), (0.7:0.3) mixtures. Furthermore, the β-Na_2ThF_6 and $NaTh_2F_9$ compounds were synthesized and subsequently analyzed with the use of X-ray diffraction. The heat capacities of both compounds were measured in the temperature ranges (2−271 K) and (2−294 K), respectively, by thermal relaxation calorimetry. Finally, a CALPHAD model coupling the structural and thermodynamic data was developed using both EMD and experimental data as input and a quasichemical formalism in the quadruplet approximation. Here, 7- and 8-coordinated Th^{4+} cations were introduced on the cationic sublattice alongside a 13-coordinated dimeric species to reproduce the chemical speciation, as calculated by EMD simulations and to provide a physical description of the melt.

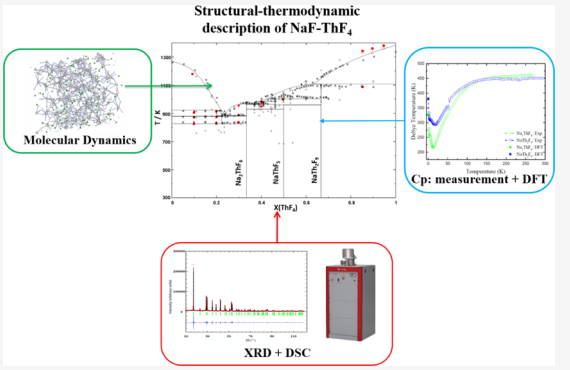

1. INTRODUCTION

From a structural viewpoint, inorganic melts can generally be classified as molecular, ionic, metallic, and network-forming, as well as having combined features from these categories.[1] In the case of molten salts, ionic, molecular, and network-forming regimes may be observed depending on the temperature and composition.[2] The LiF−BeF_2 system is a canonical example: LiF is an ionic melt, while BeF_2 is a fully connected network of bridged tetrahedral units.[3] In the process of adding BeF_2 to LiF melts, the corresponding changes in the short-range order (SRO) manifest themselves in the excess thermodynamic properties and also significantly alter the transport properties. For instance, the mechanism of electrical conductivity goes from independently diffusing ions to a mechanism where the Li^+ ions travel through channels in the network. At the same time, the viscosity increases by several orders of magnitude.[3] By and large, molten salts are thus a class of ionic liquids displaying a wide range of thermal and electrical conductivities, densities, viscosities, and melting points, among other thermophysical properties. This rich chemistry makes them ideally suited as solvents and reaction media for numerous industrial uses.

In recent times, the applications investigated include recovery of valuable metals from spent batteries,[4] carburization of steel,[5] carbon capture and storage,[6] and the production of hydrogen[7] and ammonia.[8] Yet in a 21st century facing growing energy demand in combination with the need to cut greenhouse gas emissions, one of the most promising uses of molten salts would be as fuels and coolants for a class of advanced nuclear power systems called molten salt reactors (MSRs).[9] The current reference fuel mixtures for the European molten salt fast reactor concept, LiF−ThF_4−$^{233}UF_4$ (77.5−20−2.5 mol %) and LiF−ThF_4−$^{enr}UF_4$−$(Pu,MA)F_3$ (77.5−6.6−12.3−3.6 mol %, MA = minor actinides),[10] use ^{7}LiF as the carrier salt. Interestingly, it was shown in a previous thermodynamic assessment that the addition of NaF to the LiF−ThF_4−UF_4 fuel matrix could lower the melting point of the mixture,[11] thereby limiting solidification risks and allowing for possible improvement of the overall thermodynamic efficiency of the reactor. Next to this, NaF is a significantly cheaper alternative compared to ^{7}LiF, which could be

Received: June 1, 2021
Revised: July 8, 2021
Published: July 28, 2021

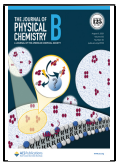

https://doi.org/10.1021/acs.jpcb.1c04830
J. Phys. Chem. B 2021, 125, 8558−8571

particularly appealing in a MSR concept operated in the fast neutron spectrum.

Accordingly, the $NaF-ThF_4$ fuel system has been investigated herein with experimental and computational methods to substantiate the knowledge on its materials' properties and the structural behavior of the melt over wide ranges of temperature and composition. The density, molar volume, thermal expansion, mixing enthalpy, heat capacity, and chemical speciation of $NaF-ThF_4$ mixtures have been calculated with molecular dynamics (MD) simulations across the entire composition space in the 1270 K < T < 2000 K range. Furthermore, the standard entropies of β-Na_2ThF_6 and $NaTh_2F_9$ have been determined using low-temperature heat capacity measurements. The mixing enthalpy of (NaF/ThF_4) = (0.8:0.2), (0.7:0.3) compositions, as well as several thermal events in the $NaF-ThF_4$ phase diagram were determined using differential scanning calorimetry (DSC). Finally, an advanced structural thermodynamic model has been developed by using MD and experimental results as input. A test of the general applicability of the model outside the parameters used to optimize it was made by calculating activities and comparing to experimental results, with satisfactory agreement.

2. METHODS

2.1. Computational Methods. *2.1.1. MD Simulations.* The polarizable ion model (PIM) model[2,12,13] was used for the MD simulations. This model, based on a semiclassical approach, has proven to be very suitable for simulating fluoride salt systems.[2,13−16] The PIM potential energy function is described by the sum of four interaction terms, including charge−charge V_{qq}, repulsion V_{rep}, dispersion V_{disp}, and polarization V_{pol} contributions. Each term is explained in Supporting Information, along with listing of the parameter values. The code used to run the simulations was PIMAIM.[12]

In general, the simulation cell consisted of approximately 600 ions (see Supporting Information). The temperatures ranged from 1270 to 2000 K. All simulations were started with a NpT run of 500 ps at 0 GPa. Depending on the properties to be calculated, the NpT run was followed by a NVT equilibration run of 200 ps and a NVT production run of 500 ps. The time steps in all ensembles were set to 0.5 fs. The Nosé-Hoover thermostat and Martyna barostat relaxation times were both set to 10 ps. The Ewald sum cutoff radius, which sets a limit to the long-range electrostatic interactions between ions, and the short-range potential cutoff radius were both set to half of the length of the simulation cell.

2.1.2. Density Functional Theory. The energy curves ($E(V)$) of Na_2ThF_6 and $NaTh_2F_9$ were calculated via DFT. For that purpose, the Vienna ab initio simulation package (VASP)[17−20] was used to perform plane-wave computations with the projected augmented wave approach[21,22] and the generalized gradient approximation of Perdew, Burke, and Ernzerhof.[23,24] Convergence in the energy and cell volume was tested and the results indicated a cutoff energy of 520 eV and 5 × 5 × 8 and 5 × 5 × 5 Γ-centered k-points grid in the first Brillouin zone for Na_2ThF_6 and $NaTh_2F_9$, respectively, with a Gaussian smearing parameter of 0.02 eV to ensure that the accuracy in the energy of the system was more than 0.01 meV. The self-consistent field convergence criterion was 1×10^{-5} eV per electronic iteration and 0.02 eV/Å for each ionic loop that was updated by the conjugate gradient approach. To calculate the energy of the equilibrium lattice, the atomic positions, cell volume, and cell shape were given freedom to relax. To calculate the energy curves, both cell volume and cell shape were fixed and only the atoms were free to move. More detailed information is found in Supporting Information.

2.2. Experimental Methods. *2.2.1. Sample Preparation.* NaF was obtained from Alfa Aesar, with 99.99% purity and was dried for 4 h at 673 K in a furnace under argon flow. The post X-ray diffraction (XRD) and DSC measurements showed no secondary phases. ThF_4 was obtained from JRC Karlsruhe. It was synthesized by fluorination of ThO_2.[25] No impurities were detected by XRD, and DSC also showed a high purity based on the melting point: (1381 ± 5) K versus 1383.0 K.[26] Because of their hygroscopic nature, all samples investigated in this work were prepared under dry argon atmosphere in a glovebox, where the oxygen and water contents were kept below 5 ppm. The DSC and XRD measurements were also done under the same protected atmosphere. The samples were sealed under an argon atmosphere in the glovebox in specifically designed tightly closed sample holders such that reactions with water or oxygen from the environment were minimized and radioactive contamination was prevented. The thermal relaxation calorimetry measurements were done under vacuum.

2.2.2. β-Na_2ThF_6 and $NaTh_2F_9$ Synthesis. NaF and ThF_4 were mixed in the appropriate stoichiometric ratios and were placed inside a nickel liner closed by a nickel lid. A stainless steel crucible enclosed the nickel assembly and was sealed with a stainless steel screw bolt. The crucible was subsequently annealed in a tubular furnace (Borel, Switzerland) up to 1423 K (above the melting point of pure ThF_4), with a 250 K/h heating ramp. A plateau of 1 h was maintained, after which the sample was slowly cooled down to room temperature with a 25 K/h cooling ramp. An argon flow was applied throughout the routine to prevent reactions with oxygen or water.

2.2.3. X-ray Diffraction. An X'pert Pro (PANAlytical) diffractometer mounted in the Bragg−Bretano configuration, with a copper anode (45 kV, 40 mA), was used for the XRD measurements. The intensities of the scattered X-rays were measured with an X'Celerator real-time multistrip detector. The angle range was set to $10° \leq 2\theta \leq 120°$ with an integration time of around 8 h and a step size of 0.008°. The purity of the synthesized compounds was checked by Le Bail refinement[27] of the XRD pattern using the FullProf software suite.[28]

2.2.4. Thermal Relaxation Measurements Using a Physical Property Measurement System. The heat capacity of the synthesized β-Na_2ThF_6 and $NaTh_2F_9$ materials was measured with a physical property measurement system (PPMS) (Quantum Design) instrument. This technique is based on the thermal relaxation method, which is described and evaluated in great detail by Lashley et al.[29] The samples were pelletized and were subsequently enclosed with a STYCAST encapsulant to prevent radioactive contamination and degradation of the hygroscopic samples. The masses of the pellets with STYCAST were 13.2 mg (10.3 mg without) for β-Na_2ThF_6 and 12.7 mg (10.9 mg without) for $NaTh_2F_9$. The contributions of the grease, platform, heater, wires, and temperature sensor were measured in a separate run prior to the measurement of the heat capacity of the actual sample (the addenda curve). The addenda and STYCAST heat capacity contributions were then subtracted from the measured values of the sample run. The heat capacity was measured between 2 and 271 K for β-Na_2ThF_6 and between 2 and 294 K for $NaTh_2F_9$. No magnetic field was applied during the experiments. Based on the experience with the PPMS instrument and

https://doi.org/10.1021/acs.jpcb.1c04830
J. Phys. Chem. B 2021, 125, 8558−8571

Table 1. Thermodynamic Data for End Members and Intermediate Compounds Used in This Work for the Phase Diagram Assessment: $\Delta_f H^o_m$ (298 K)/(kJ·mol^{-1}), S^o_m (298 K)/(J·K^{-1}·mol^{-1}), and Heat Capacity Coefficients $C_{p,m}$ (T/K)/(J·K^{-1}·mol^{-1}), where $C_{p,m}$ (T/K) = $a + b{\cdot}T + c{\cdot}T^2 + d{\cdot}T^{-2}$[a]

			$C_{p,m}$ (T/K)/(J·K^{-1}·mol^{-1}) = $a + b{\cdot}T + c{\cdot}T^{-2}$			
compound	$\Delta_f H^o_m$ (298 K)/(kJ·mol^{-1})	S^o_m (298 K)/(J·K^{-1}·mol^{-1})	a	b	c	refs
NaF(cr)	−576.650	51.21	47.63	1.479 × 10^{-2}	−464,300	45
NaF(l)	−557.730	52.755	72.989			45
ThF_4(cr)	−2097.900	142.05	111.46	2.6900 × 10^{-2}	−780,000	26,46
ThF_4(l)[b]	−2100.360	106.61	168.0			26,46
Na_4ThF_8(cr)	**−4360.695**	**436.4**	301.98	8.6060 × 10^{-2}	−2,637,200	this work
$Na_7Th_2F_{15}$(cr)	**−8272.950**	**675.6**	556.33	1.5733 × 10^{-1}	−4,810,100	this work
Na_2ThF_6(cr)	**−3276.100**	257.3	**207.5043**	**4.5076×10^{-2}**	**−1,824,833**	this work
$Na_3Th_2F_{11}$(cr)	**−5899.800**	**525.0**	365.81	9.8170 × 10^{-2}	−2,952,900	this work
$Na_7Th_6F_{31}$(cr)	**−16689.725**	**1300.0**	1002.17	2.6493 × 10^{-1}	−7,930,100	this work
$NaThF_5$(cr)	**−2696.500**	**194.2**	159.09	4.1690 × 10^{-2}	−1,244,300	this work
$NaTh_2F_9$(cr)	**−4808.106**	333.7	**287.165**	**2.7885×10^{-2}**	**−2,574,616**	this work

[a]Optimized data are shown in bold. [b]ThF_4(l) is modeled as a [$Th_{VII}F_4$(l)−$Th_{VIII}F_4$(l)−$Th_{2[XIII]}F_8$(l)] mixture with $g^0_{Th_{[VII,VIII]}F_4}(l) = \frac{1}{2}g^0_{Th_{2[XIII]}F_8(l)}$ + 150,000 J·mol^{-1}.

the encapsulation of similar materials in STYCAST,[30,31] the uncertainty of the measurements was estimated to be 3% for temperatures lower than 100 K and 1% between (100 and 300 K). Treatment of the data was done as outlined in section and described at length in refs 32−34.

2.2.5. Phase Equilibrium Measurements by DSC. The transition temperatures were measured using a Setaram multidetector high-temperature calorimeter (MHTC-96 type) operating in the DSC mode, equipped with S-type thermocouples, capable of measuring up to 1673 K.

NaF−ThF_4 mixtures were placed in a nickel liner. A stainless-steel crucible encapsulated the liner, and a nickel lid was pressed into the liner by screwing a stainless steel bolt onto the crucible such that the sample was hermetically sealed from the environment, as in ref 35 (see Supporting Information also). The transition temperatures were measured for the compositions (NaF/ThF_4) = (0.9:0.1), (0.8:0.2), (0.7:0.3), (0.6:0.4), (0.5:0.5), (0.15:0.85), (0.1:0.9), and (0.05:0.95). For every experiment, four heating cycles were applied, in which the sample was annealed approximately 90 K above the melting points of the end members during the first cycle and above the liquidus line for the subsequent cycles, as seen in the reported phase diagrams.[11,36] Subsequently, the recorded temperatures assigned to a particular event were averaged over the successive cycles, excluding the first one. The measured temperatures were corrected with a temperature calibration equation, derived by measuring the melting points of different high-purity metallic standards (In, Pb, Sn, Al, Ag, and Au) following the procedure described in refs 37 and 38. The uncertainty on the measured temperatures is estimated to be 5 K for pure compounds and 10 K for mixtures. The onset temperature obtained by tangential analysis of the heat flow was selected for transitions and congruent melting temperatures. The extremum of the heat flow peak was selected for the liquidus events, as recommended by Boettinger et al.[39]

2.2.6. Enthalpy of Mixing Measurements by DSC. Mixing enthalpy experiments were performed with the same type of crucibles as used in the DSC measurements. The technique and determination of the detector sensitivity are described in great detail in ref 40 (see Supporting Information as well). A pellet of NaF was placed below a ThF_4 pellet. A small nickel liner separated the end-member compounds such that eutectic melting or solid-phase reactions were prevented until melting of NaF, which initiated the mixing event. Au reference material (>99.99% purity) was measured at the same time as the sample, which allowed us to determine the detector sensitivity and subsequently the total enthalpy involved in the mixing event $\Delta_{meas}H^o_m(T_{fus,NaF})$. The enthalpy of mixing is then calculated by subtracting the fusion enthalpies of the end members from the measured heat

$$\Delta_{mix}H^o(T_{fus,NaF}) = \Delta_{meas}H^o(T_{fus,NaF}) - x_{NaF}\Delta_{fus}H^o(KF, T_{fus,NaF}) - x_{ThF_4}\Delta_{fus}H^o(ThF_4, T_{fus,NaF}) \quad (1)$$

The samples were heated beyond the melting point of ThF_4 to check if any material remained unreacted.

Note that it is assumed that the fusion enthalpy of ThF_4 is temperature-independent and is thus the same at the melting temperature of NaF. This is a reasonable approximation according to the work of Capelli et al.[40] The fusion enthalpies used were 36.4 kJ mol^{-1} for ThF_4[10] and 33.3 kJ mol^{-1} for NaF.[41] The uncertainties in the mixing enthalpy $\Delta_{mix}H^o_m(T_{fus,NaF})$ were determined from the standard uncertainty of the calibration process. The setup was the same as the one used to measure mixing enthalpies in the KF−ThF_4 system, with which the fusion enthalpies of LiF, NaF, KF, and ThF_4 were measured within experimental error.[42]

2.3. CALPHAD Modeling. *2.3.1. Pure Compounds.* The optimization of the NaF−ThF_4 thermodynamic model was carried out using the FactSage software[43] (Version 7.2). To assess a phase diagram, the identity of the phases present in the system of interest must be known, as well as their respective Gibbs energy functions. In this work, the Neumann−Kopp rule[44] was used to approximate the heat capacities of intermediate compounds in the absence of experimental data, with the exception of β-Na_2ThF_6 and $NaTh_2F_9$. For each of these two phases, a polynomial fit bridging the measured low-temperature heat capacity data (~2 to ~298 K, section) and behavior at high temperatures (500 K to melting point) as predicted by the Quasi-Harmonic Approximation (QHA) was used. The thermodynamic data for all compounds in this study are listed in Table 1. The data for solid and liquid NaF and

https://doi.org/10.1021/acs.jpcb.1c04830
J. Phys. Chem. B 2021, 125, 8558−8571

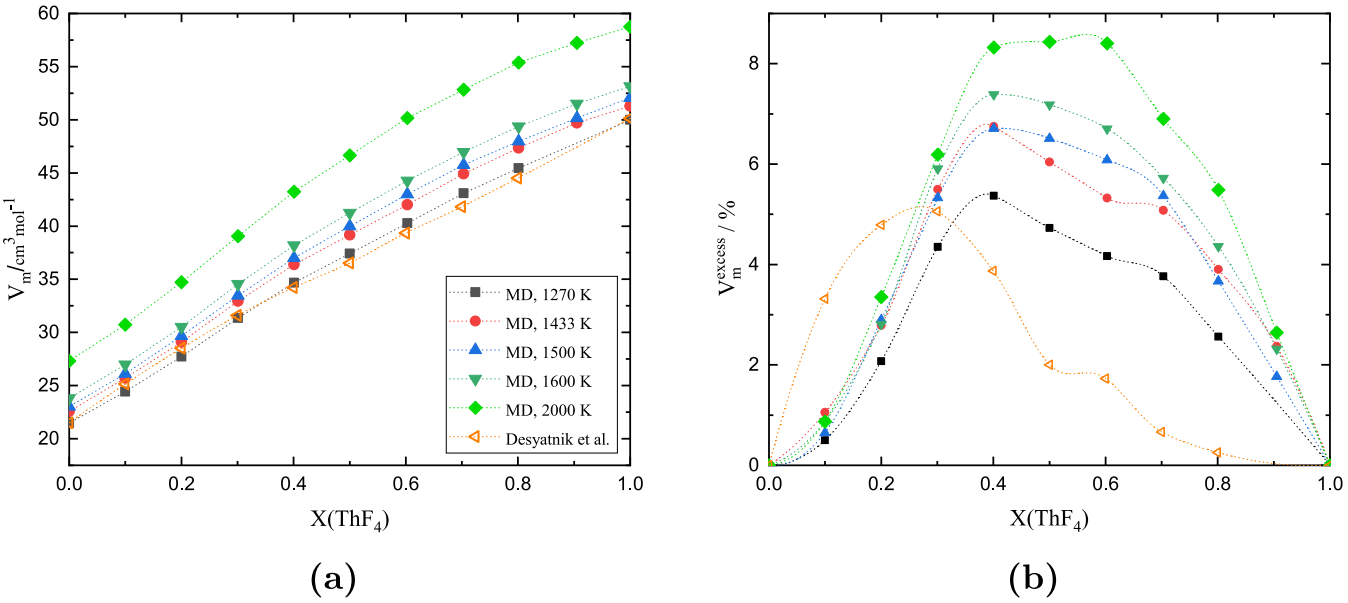

Figure 1. (a) Molar volumes versus composition at T = 1270, 1433, 1500, 1600, and 2000 K. (b) Excess molar volumes versus composition at the same temperatures. Both are compared to data by Desyatnik et al.[52] at 1270 K.

ThF_4 were taken from NIST-JANAF[45] and the work by Tosolin et al.[46] and Konings and van der Meer,[26] respectively. The standard enthalpies of formation and standard entropies of all the intermediate compounds were optimized to closely match phase equilibria data and thermodynamic data reported herein (mixing enthalpies, standard entropies of α-Na_2ThF_6 and $NaTh_2F_9$).

2.3.2. Liquid Solution. The excess Gibbs energy terms of the $(Na,Th)F_x$ liquid solution have been modeled in the present work using a modified quasi-chemical model similar to the one recently optimized for the LiF−BeF_2 system.[47] A detailed description is given in Supporting Information. As will be examined in the following sections, $(Na,Th)F_x$ is not a solution in which cations and anions are completely dissociated. Rather, the solution is formed by discrete coordination complexes of F^- ligands around Th^{4+}. At low ThF_4 concentrations, most Th^{4+} are present as monomers, primarily with coordination numbers 7 and 8: $[ThF_7]^{3-}$ and $[ThF_8]^{4-}$. Hence, in this work, two distinct Th^{4+} cations were taken into account: $Th^{4+}_{[VII]}$ and $Th^{4+}_{[VIII]}$. At higher ThF_4 concentrations, the number density of the monomers increases, leading to dimers $[Th_2F_x]^{8-x}$, trimers $[Th_3F_y]^{12-y}$, and longer chains or "polymers" of thorium cations linked together by bridging fluorides (see Figure 5). There are many chain lengths possible, not all of which can be taken into account if the number of fitting parameters is to be kept from becoming too large. Hence, dimers and all species of higher nuclearity were included in the model as dimers in which the overall coordination sphere around the two Th atoms is made of 13 fluorine atoms (the most abundant according to MD simulations), with the corresponding cation $Th^{8+}_{2[XIII]}$. Given that pure ThF_4(l) is a network of mostly corner-sharing coordination polyhedra ,[48,49] it was modeled as a solution of dimers. Such a choice is a simplification, yet one which already reflects a main structural characteristic of the network: fluoride bridging. A detailed description of the complete model as well as the optimized parameters are provided in Supporting Information.

2.3.3. Solid Solution. A solid solution appears in the system in the ThF_4-rich side of the phase diagram according to Thoma et al.,[50] although earlier work by Emelyanov and Evstyukhin[51] did not find evidence of the solid solution. The DSC data in this work do not give conclusive evidence on the matter. The solid solution phase was thus not retained in this work.

3. RESULTS AND DISCUSSION

3.1. Structural Investigations of the $(Na,Th)F_x$ Melt via MD. *3.1.1. Density and Molar Volume.* The densities ρ and molar volumes V_m (Figure 1a) of the $(Na,Th)F_x$ melt were calculated with MD from the mean volume of the cubic simulation cells after the NpT run at 1270, 1433, 1500, 1600, and 2000 K over the full concentration range. The results at 1270 K are compared to the experimental data obtained by Desyatnik et al.[52] (for the mixtures) and Kirschenbaum and Cahill[53] (for pure ThF_4) by interpolating at the same temperature. A maximum relative deviation of less than 3% is observed; hence, good agreement was found between the calculated density data using MD and the experimental values, especially when considering the fact that experimental works on densities of salt mixtures can vary by several percent.[9]

The molar volume increases quasi-linearly with increasing concentration of ThF_4 and increases with temperature, as expected. The excess molar volume is shown in Figure 1b. A positive excess molar volume is observed for the MD and experimental data. The local maximum at T = 1270 K is at 40 mol %, slightly shifted compared to the maximum of the experimental data (30 mol %). The magnitude of the excess is similar in that region, close to 5%. As the temperature is increased, the excess molar volume grows. The maxima of the MD calculated curves are reached at approximately 40 mol % ThF_4 for all temperatures, which coincides with the complete polymerization of the melt (see Figure 5).

3.1.2. Order at Short Range. Fluoride melts display strong SRO, with a coordination environment of fluorides around cations and vice versa. The coordination numbers of the $[ThF_n]^{m-}$ complexes in the melt were calculated from the radial distribution functions $g(r)$ (RDF) of the Th−F pair.

https://doi.org/10.1021/acs.jpcb.1c04830
J. Phys. Chem. B 2021, 125, 8558−8571

Here, the output of the *NVT* production runs over the full composition range at 1270, 1433, 1500, and 1600 K were used. The Th−F RDF at 70 mol % ThF_4 composition at 1500 K is shown in Figure 2 (black line). The first minimum occurs

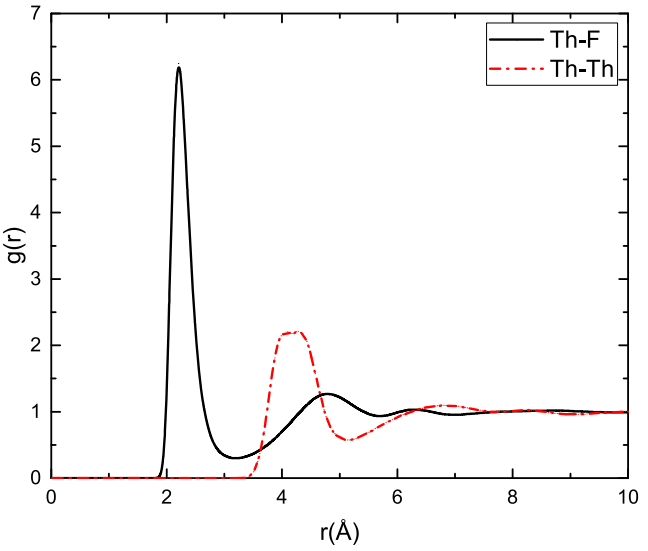

Figure 2. RDF of Th−F and Th−Th bonds at 70 mol % ThF_4 at 1500 K, shown in black and red, respectively.

around 3.17 Å. The Th−Th RDF is also shown in Figure 2 (red line). The first minimum occurs around 5.10, representing the radius of the second coordination shell. The first local minimum in the Th−F RDF was taken as the cutoff radius of the first coordination shell. Hence, the coordination numbers were determined by counting the number of F^- anions within the radius of the first coordination shell of a Th^{4+} cation.

The calculations reveal coordinations of 6, 7, 8, 9, and 10, with 7, 8 and 9 being the predominant ones. Figure 3 shows the distribution of the 7-, 8-, and 9-coordinated $[ThF_n]^{m-}$ complexes in the melt. In general, $[ThF_8]^{4-}$ and $[ThF_9]^{5-}$ become more dominant as the concentration of ThF_4 increases. The increase in fractions of 8- and 9-coordinated $[ThF_n]^{m-}$ complexes was also observed in different studies in the high thorium concentration region for the LiF−ThF_4 system[15,48,54] and is related to the formation of a molecular network (see below). Furthermore, the predominance of 8-coordinated complexes and the substantial presence of 7-coordinated complexes, as found in this work, was also observed experimentally with Raman spectroscopy in LiF−NaF−ThF_4 melts.[55] As the temperature increases, the relative fractions of 7- and lower-coordinated complexes increase. The same phenomenon was also observed during investigations on the LiF−ThF_4 system.[15] Bond rearrangement is facilitated at higher temperatures due to the increased kinetic energies of the ions, and thus, the fraction of higher-coordinated complexes is smaller.

The average coordination number of $[ThF_n]^{m-}$ complexes versus composition in the NaF−ThF_4 melt is shown for various temperatures in Figure 4. It decreases with temper-

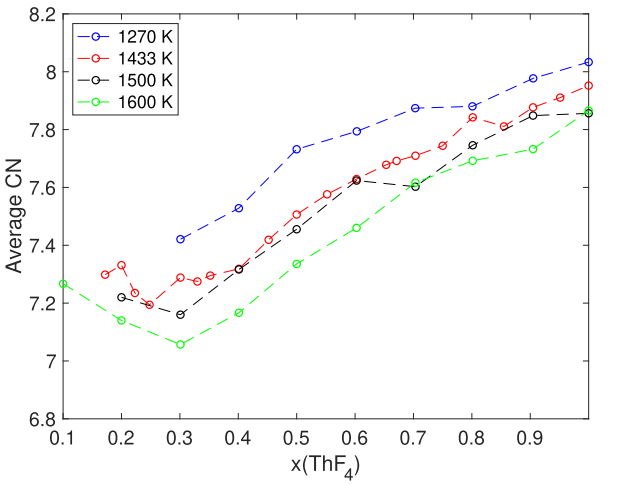

Figure 4. Evolution of the average coordination numbers of $[ThF_n]^{m-}$ complexes versus composition in the NaF−ThF_4 system at various temperatures.

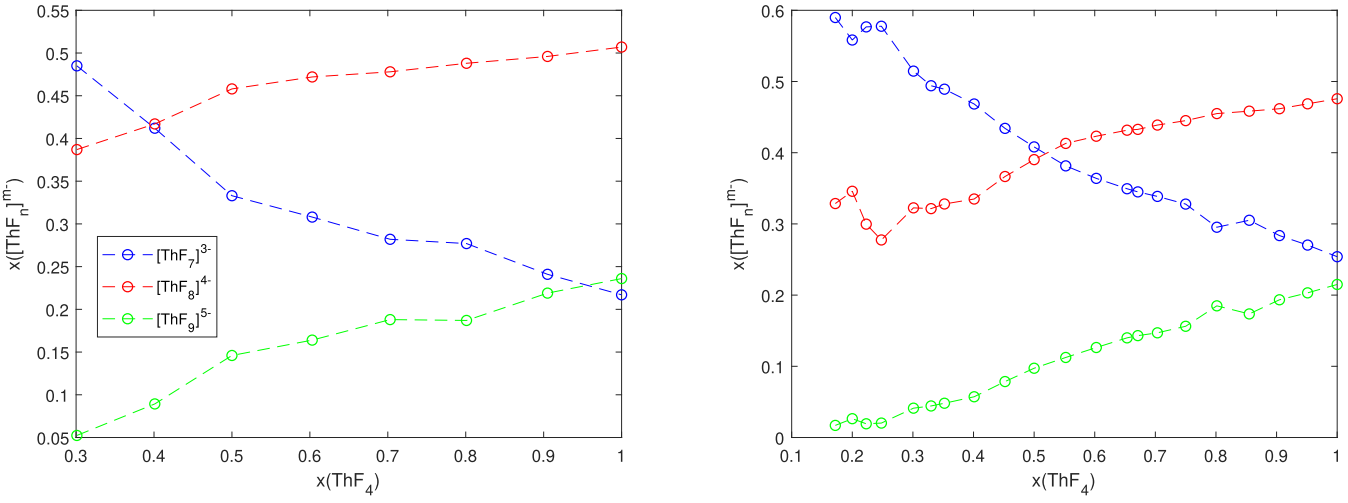

Figure 3. Distribution of the 7-, 8-, and 9-coordinated $[ThF_n]^{m-}$ complexes versus composition in the NaF−ThF_4 system at 1270 (supercooled at $X(ThF_4) > 0.8$) and 1433 K.

https://doi.org/10.1021/acs.jpcb.1c04830
J. Phys. Chem. B 2021, 125, 8558−8571

ature, due to a lower proportion of 8- and 9-coordinated complexes at higher temperatures. It increases gradually in the region 30−100 mol % ThF_4. The calculations at 1500 and 1600 K reveal a minimum in the average coordination numbers around 30 mol % ThF_4. The lower average coordination number indicates that smaller complexes form, which allow for more densely packed arrangements, and hence results in a higher density and lower molar volume.

3.1.3. Medium-Range Order in the (Na,Th)F_x Liquid Solution. An advantage of MD simulations is that a detailed description of the structure of the salt is obtained at length scales accessible with total neutron/XRD,[56] that is, beyond those accessible with other experimental techniques, for example, XAS and Raman spectroscopy. For example, links between thorium cations via fluoride bridging can be subject to analysis. Two thorium centers, separated by a distance r, are said to be fluoride-bridged if $r < R_{Th-Th,cutoff}$ and $r < 2 \cdot R_{Th-F,cutoff}$. $R_{Th-Th,cutoff}$ and $R_{Th-F,cutoff}$ denote the first local minima in the Th−Th and Th−F RDFs, respectively. Dimers, trimers, and species of higher nuclearity thus arise from fluoride bridging, up to the point where a network may emerge.

It has been observed that alkali cations, depending on their nature and concentration, can significantly impact the network-forming abilities of ionic systems due to steric effects.[57,58] Na^+ is small enough to allow for the complexes to link via bridging fluorides and form a network, as can be seen in Figure 5. The

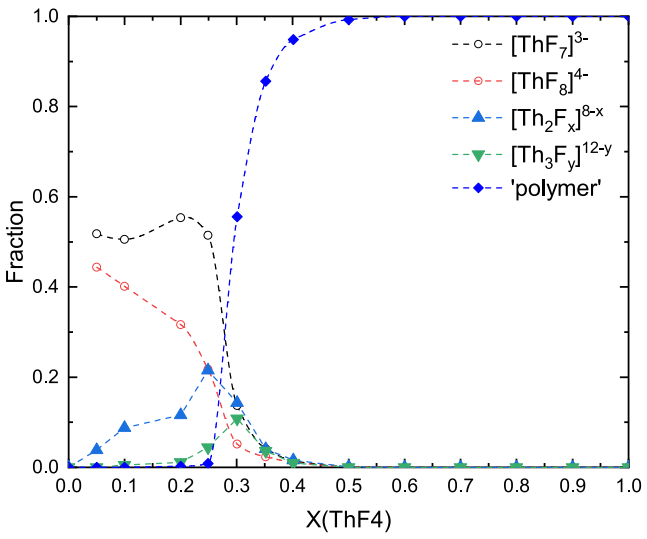

Figure 5. Fraction of monomers (○), dimers (♦), and "polymers" (▲) in the NaF−ThF_4 liquid solution at T = 1433 K.

species are classified into three groups, namely, monomers (ThF_x^{4-x}), dimers ($Th_2F_x^{8-x}$), and "polymers", that is, any chain where three or more Th^{4+} ions are linked together. The behavior is very similar across temperatures (see Supporting Information): with increasing ThF_4 content, there is a monotonic decrease and increase of the monomer and polymer fractions, respectively, while the concentration of dimers reaches a maximum in the region $0.2 < X(ThF_4) < 0.25$. In the same region, Desyatnik et al.[52] found a local maximum of the viscosity, which the authors attributed to the specific stability of $[ThF_7]^{3-}$ complexes. The structural properties emerging from the MD simulations suggest that it is not only the single shells but also their dimers which have a large contribution to the viscosity at that composition range.

3.2. Thermodynamic Studies. *3.2.1. Phase Diagram Investigations.* To date, experimental data on the NaF−ThF_4 system are only available from a handful of studies. Zachariasen published a series of papers in 1948−1949 reporting the existence of the Na_4ThF_8, Na_2ThF_6 and $NaTh_2F_9$ intermediates.[59] In other studies, the author reported that four polymorphs existed for the Na_2ThF_6 compound.[60,61] Later, Emelyanov and Evstyukhin[51] investigated the phase equilibria and identified four phases: Na_4ThF_8, Na_2ThF_6 (with a phase transition), $NaThF_5$, and $NaTh_2F_9$. Making use of a wider set of experimental techniques, Thoma et al.[50] also assessed the system and included six compounds in their description: two congruently melting phases, namely, Na_2ThF_6 (without polymorphism) and $Na_3Th_2F_{11}$, as well as four other compounds: Na_4ThF_8, $Na_7Th_6F_{31}$, $NaThF_5$, and $NaTh_2F_9$. Making use of quenching techniques, the authors subsequently identified the $Na_7Th_2F_{15}$ compound.[62]

More modern investigations by Grzechnik et al. provide a complete overview of structural properties of the β-Na_2ThF_6[63] and $NaTh_2F_9$[64] intermediates. Grzechnik et al. detected no phase transitions for β-Na_2ThF_6 in the temperature range 290−954 K nor did Mukherjee and Dash[36] in a recent experimental determination of the standard thermodynamic functions and melting point of this intermediate. A DSC scan of the synthesized β-Na_2ThF_6 in the present work was performed to see if transitions to other phases occur. However, only a congruent melting point was detected, in line with Thoma et al., Grzechnik et al., and Mukherjee et al. Moreover, there is no evidence of a phase transition in the low-temperature heat capacity data (see section below), so Na_2ThF_6 has only one phase from 0 K until its melting point. Data are scarcer on the phase equilibria at high ThF_4 content. In this region, the phase $NaTh_3F_{13}$ has also been reported, synthesized via a hydrothermal route by Underwood et al.[65] and characterized with single-crystal XRD. The melting point or other thermodynamic data were not measured. It is likely to be metastable, as previous investigations of the system did not find evidence for it, and indeed, none of the DSC measurements in this work (Table 2) seem to indicate that it is stable.

Figure 12 shows a great agreement between events measured in this work and the present description of the NaF−ThF_4 phase diagram in the region $x(ThF_4) \leq 0.33$. In the $0.33 < x(ThF_4) < 0.67$ region, there is a higher uncertainty. The eutectoid at 881 K, $x(ThF_4) = 0.401$, was not observed, and only one event was measured at $x(ThF_4) = 0.497$, which could indicate congruent melting of $NaThF_5$. Furthermore, another sample was made from the $x(ThF_4) = 0.497$ composition, which was annealed up to 1423 K and analyzed using XRD, following the same procedure as the syntheses of β-Na_2ThF_6 and $NaTh_2F_9$, described previously in the Methods section. The Bragg reflections of the XRD pattern matched with the crystallographic data of ref 50 for $NaThF_5$, suggesting that $NaThF_5$ is stable from room temperature up to the point of congruent melting. However, more crystallographic investigations are needed to confirm this.

The region between 85 and 100 mol % is characterized by the presence of a solid solution according to Thoma et al.[50] However, there is little experimental data confirming its existence. Therefore, measurements were done at $x(ThF_4) = 0.853$, 0.897, 0.947. The peritectic at $x(ThF_4) = 0.853$, T =

https://doi.org/10.1021/acs.jpcb.1c04830
J. Phys. Chem. B 2021, 125, 8558−8571

Table 2. Phase Equilibria in the NaF−ThF_4 System Measured Using DSC in This Work[a]

$x(ThF_4)$[a]/mol %	T/K	equilibrium	invariant reaction
9.9	825.0	eutectoid	NaF + Na_2ThF_6 = $Na_7Th_2F_{15}$
9.9	870.3	eutectoid	$Na_7Th_2F_{15}$ + NaF = Na_4ThF_8
9.9	905.2	peritectic	Na_4ThF_8 = L + NaF
9.9	1178.7	liquidus	NaF + L′ = L
19.9	829.0	eutectoid	$Na_7Th_2F_{15}$ + NaF = Na_4ThF_8
19.9	872.3	eutectoid	$Na_7Th_2F_{15}$ + NaF = Na_4ThF_8
19.9	912.8	peritectic	Na_4ThF_8 = L + NaF
29.8	834.8	eutectoid	NaF + Na_2ThF_6 = $Na_7Th_2F_{15}$
29.8	886.2	eutectic	$Na_7Th_2F_{15}$ + Na_2ThF_6 = L
29.8	951.6	liquidus	Na_2ThF_6 + L′ = L
33.3	966.5	liquidus	Na_2ThF_6 = L
40.1	949.4	eutectic	Na_2ThF_6 + $Na_3Th_2F_{11}$ = L
40.1	978.9	peritectic	$Na_7Th_6F_{31}$ + L = $Na_3Th_2F_{11}$
49.7	998.4	peritectic	$Na_7Th_6F_{31}$ = L + $NaTh_2F_9$
85.3	1086.4	peritectic	$NaTh_2F_9$ = L + ThF_4
85.3	1343.3	liquidus	ThF_4 + L′ = L
89.7	1360.0	liquidus	ThF_4 + L′ = L
94.7	1379.2	liquidus	ThF_4 + L′ = L
1.0	1381.0	congruent melting	ThF_4 = L

[a]Standard uncertainty $u(x(ThF_4))$ = 0.5 mol %.

1086.4 K, was observed as well as the liquidus equilibrium at this composition. The presence of a solid solution was not detected in the measurements at $x(ThF_4)$ = 0.897 and 0.947 using DSC. Hence, further investigations are needed to confirm its existence, using, for instance, high-temperature XRD analysis or quenching techniques.

3.2.2. XRD Analysis. The XRD patterns of β-Na_2ThF_6 and $NaTh_2F_9$ are shown in Figures 6 and 7, respectively. No

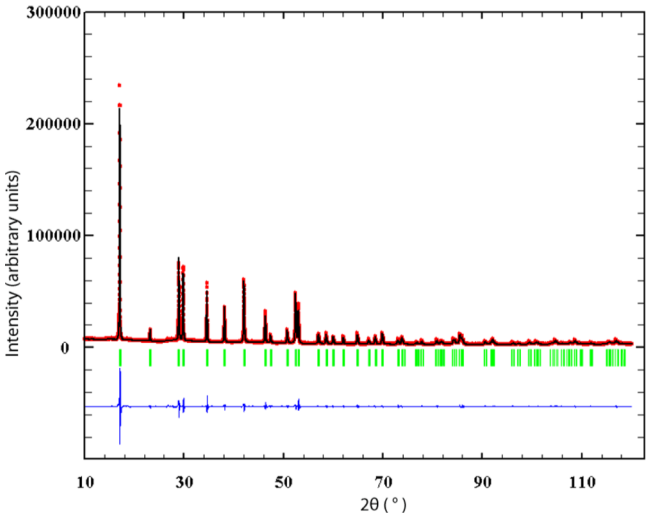

Figure 6. Comparison between the observed Y_{obs} (red) and calculated Y_{calc} (black) XRD pattern of $NaTh_2F_9$. $Y_{obs} - Y_{calc}$ (blue) is the difference between the experimental and calculated intensities. The Bragg reflections' angular positions are marked in green. Measurement at λ = Cu-Kα.

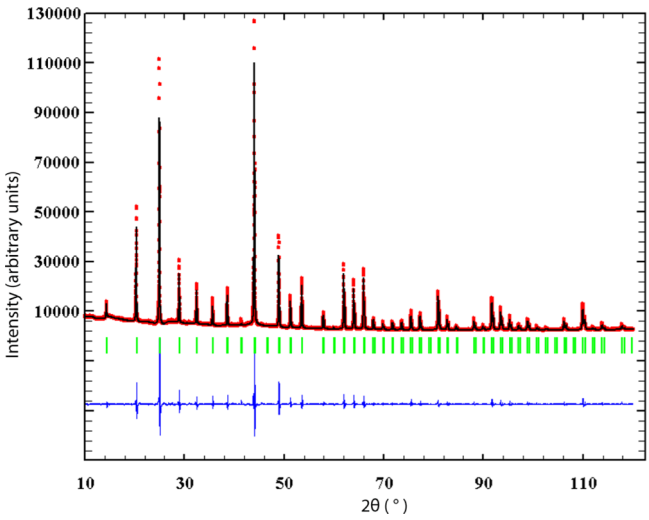

Figure 7. Comparison between the observed Y_{obs} (red) and calculated Y_{calc} (black) XRD pattern of β-Na_2ThF_6. $Y_{obs} - Y_{calc}$ (blue) is the difference between the experimental and calculated intensities. The Bragg reflections' angular positions are marked in green. Measurement at λ = Cu-Kα.

secondary phases were detected, and the purity was estimated to be >99%. The patterns were refined using the Le Bail method.[66] The refined values of the cell parameters of both compounds are given in Table 3. Good agreement was found

Table 3. Cell Parameters of Refined XRD Patterns

compound	space group	a/Å	b/Å	c/Å
β-Na_2ThF_6	$P321$ (150, trigonal)	5.983(3)	5.983(3)	3.833(5)
$NaTh_2F_9$	$I\bar{4}2m$ (121, tetragonal)	8.723(9)	8.723(9)	8.724(2)

with the cell parameters for β-Na_2ThF_6 and $NaTh_2F_9$ at ambient temperature and pressure reported by Grzechnik and co-workers, given by a = 5.985(2) Å, b = 5.985(2) Å, and c = 3.843(1) Å for β-Na_2ThF_6 with the space group $P321$ (150)[63] and a = 8.763(1) Å, b = 8.763(1)Å, and c = 8.640(2) Å for $NaTh_2F_9$[64] with the space group $I\bar{4}2m$ (121).

3.2.3. Low-Temperature Heat Capacity. Low-temperature heat-capacity data at constant pressure, $C_P = (\partial H/\partial T)_P$, were measured for β-Na_2ThF_6 and $NaTh_2F_9$ with thermal relaxation calorimetry between 2−271 and 2−294 K, respectively. Even though C_P is measured at low temperatures, it is in principle possible to extrapolate to higher temperatures via atomistic-scale simulations. The thermodynamic properties of stoichiometric compounds can be calculated by combining DFT with the QHA method (see Supporting Information also).[67] It has been shown,[32,68] however, that the QHA method leads to an overestimation of the heat capacity at high temperature induced by an overestimation of the lattice expansion. To alleviate this inconsistency, Seifitokaldani and Gheribi[32−34] developed the so-called thermodynamically self-consistent (TSC) method, which is based on the QHA method but with an optimization of the volume-dependent Debye temperature through a rigorous minimization procedure in order to satisfy the Maxwell relations. Here, we propose to combine the experimental information on low-temperature heat capacity with DFT simulations for an accurate parameterization of the quasi-harmonic Gibbs energy, treating both ternary salts as insulators.

https://doi.org/10.1021/acs.jpcb.1c04830
J. Phys. Chem. B 2021, 125, 8558−8571

The heat capacity of insulating materials is of vibrational origin and can be represented by the Debye−Grüneisen model,[69] described by two parameters: the Debye temperature, Θ_D, and the Grüneisen parameter, γ. Note that the Grüneisen parameter describes the volume dependence of the Debye temperature as $\gamma = (\partial \ln \Theta_D/\partial \ln V)$. At high temperature, for instance, $T > 0.75 \times T_{fusion}$, defects (e.g., Schottky) may contribute significantly to the heat capacity. The defect contribution to the heat capacity increases exponentially with temperature and its magnitude depends on the energy of formation of defects. However, experiments on high-temperature heat capacity of alkali fluoride-actinide fluoride compounds[70] show no significant contribution from the defects; therefore, it can be reasonably assumed that the heat capacities of both Na_2ThF_6 and $NaTh_2F_9$ are uniquely of vibrational nature.

According to the Debye model, the vibrational heat capacity at constant volume can be described by

$$C_V = 3NR\int_0^{\theta_D/T} \frac{e^x x^4}{(e^x - 1)^2}\cdot dx \quad (2)$$

with N being the number of atoms in the formula unit and R being the gas constant. Then, the heat capacity at constant pressure is expressed as

$$C_P = C_V(1 + \alpha\gamma T) \quad (3)$$

α being the volumetric thermal expansion coefficient. Note that the QHA, with parameters derived either from DFT or from experimental elastic properties, cannot predict the intrinsic anharmonic effect upon the lattice vibration, especially at low temperatures[69,71] (extrinsic anharmonicity can be predicted by QHA through thermal expansion contribution). The combination of QHA and experimental measurement of C_P, even in a narrow range of temperature, can on the one hand provide valuable information on the anharmonic nature of the lattice vibration within the solid and on the other hand significantly improve the accuracy in the representation of the temperature dependence of the heat capacity and the prediction of other equilibrium properties: thermal expansion and bulk modulus, among others.

First, the Debye temperature and the Grüneisen parameter were calculated at 0 K via DFT according to the methodology described in refs 32−34 (see Supporting Information also). Then, the Debye temperature was calculated numerically at each measurement temperature to fit the heat capacity, as measured in this work. The evolution of the Debye temperatures of both compounds as a function of temperature is shown in Figure 8. The behavior of the Debye temperature is similar for both compounds. A similar behavior is observed for several insulating materials and semiconductors:[69,71] at low temperature, the Debye temperature decreases to reach a minimum (here, at around 20 K), and then, it increases to reach a plateau at around $\theta_D(\infty)/4$. Without any intrinsic anharmonic effect, the Debye temperature shows no temperature dependence. Even though several analytical expressions for the description of the temperature dependence of the Debye temperature are proposed in the literature, the focus here is on the qualitative behavior: both Na_2ThF_6 and $NaTh_2F_9$ show an anharmonic behavior at low temperature and become harmonic above around $\theta_D(\infty)/4$. A consequence of the harmonic behavior at higher temperature can be observed from the quasi linear increase of C_P with temperature.

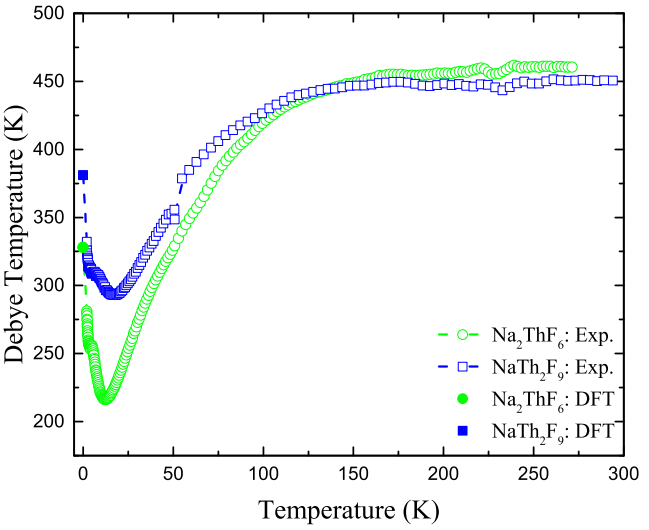

Figure 8. Temperature-dependent Debye temperature derived from experimental heat capacity (Exp., open symbol) for Na_2ThF_6 and $NaTh_2F_9$ compounds. The 0 K Debye temperatures determined by DFT for both compounds are represented by solid symbols).

At high temperature, the harmonic heat capacity at constant volume, C_V, tends to be beyond the Dulong−Petit limit of $3nR$ since the slope of the C_P induced by harmonic vibration within the crystal is around $\alpha\gamma$ (eq 3). Above this threshold temperature, the increase of C_P is linear, mainly due to the lattice expansion ($C_V\alpha\gamma T$). It is interesting to note the good interpolability between the Debye temperature at 0 K obtained by DFT and those derived from the measured C_P. The high temperature limits of the Debye temperatures for both Na_2ThF_6 and $NaTh_2F_9$ are very close, that is, 450−460 K. At low temperature, the Debye temperature of Na_2ThF_6 is significantly lower than that of $NaTh_2F_9$, indicating a more pronounced anharmonicity for Na_2ThF_6 at low temperature.

The heat capacities calculated by the TSC method, considering the Debye temperature derived from the experimental measurements, are represented in Figure 9 from 0 K up to the melting temperature and compared to the

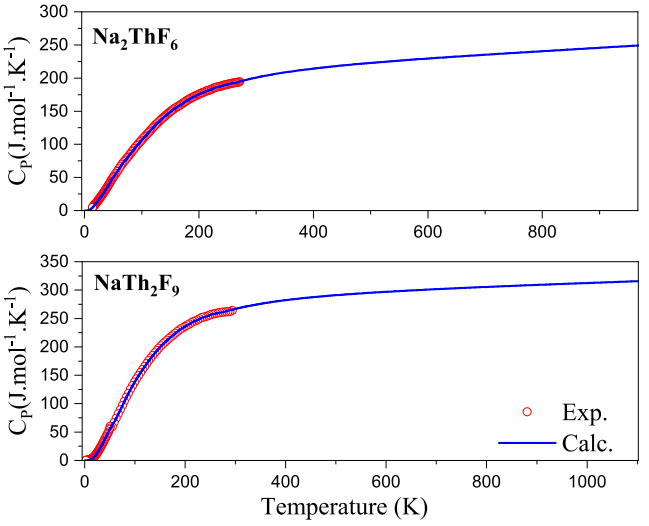

Figure 9. Experimental vs calculated heat of Na_2ThF_6 and $NaTh_2F_9$ compounds from 0 K up to the melting temperature.

https://doi.org/10.1021/acs.jpcb.1c04830
J. Phys. Chem. B 2021, 125, 8558−8571

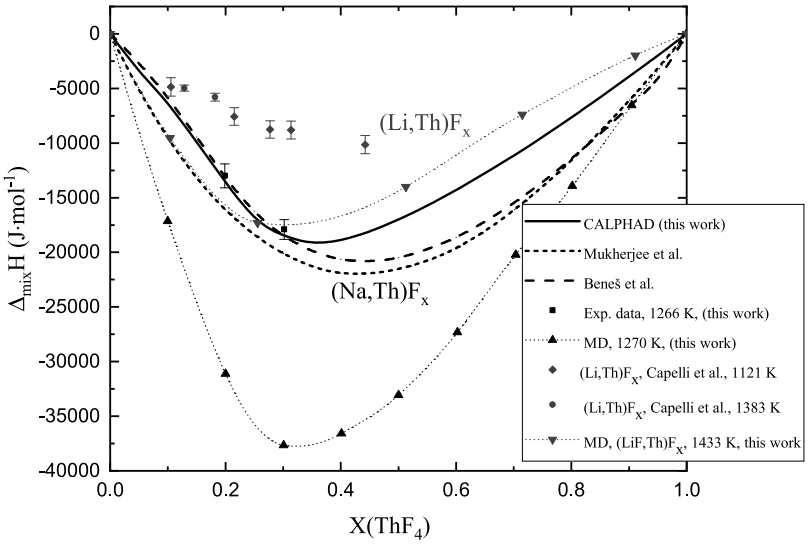

Figure 10. Mixing enthalpies in the NaF−ThF_4 system measured in this work at T = 1266 K (■) compared with the present model, those of Beneš et al.[11] and Mukherjee and Dash[36] (black lines), and the MD simulations at 1270 K (this work, ▲). Also plotted are experimentally measured values in the LiF−ThF_4 system[40] (●, blue, T = 1383 K, ♦, T = 1121 K) and values obtained via MD simulations (▼, T = 1433 K).

measured low temperature data. To extrapolate the heat capacity at higher temperatures, we have assumed that (i) the Debye temperature is constant above 200 K and (ii) the Grüneisen parameter is assumed to be independent of temperature and equal to the DFT value (1.61 for Na_2ThF_6 and 1.56 for $NaTh_2F_9$). Values of $C_{p,m}$ (298.15 K) = (200.4 ± 2.0) J K^{-1} mol^{-1} and (266.5 ± 2.7) J K^{-1} mol^{-1} were obtained from our model for β-Na_2ThF_6 and $NaTh_2F_9$, respectively. Upon integration of $C_{p,m}/T$, the corresponding standard entropies were S^o_m (298.15 K) = (257.3 ± 3.2) J K^{-1} mol^{-1} and S^o_m (298.15 K) = (333.7 ± 4.0) J K^{-1} mol^{-1}. The predicted thermal expansion coefficients of both Na_2ThF_6 and $NaTh_2F_9$ are reported in Supporting Information of this paper.

The heat capacity of Na_2ThF_6 was measured from 313 to 773 K by Mukherjee and Dash[36] using a heat flux-type DSC. However, the heat capacity data reported by Mukherjee and Dash[36] is likely too low as at a high temperature (near the melting point), the heat capacity is much lower than the Dulong−Petit approximation (Figure 3 of their paper), which is a nonphysical behavior. No comparison with their heat capacity data will be further discussed here.

3.2.4. Mixing Enthalpy in the NaF−ThF_4 System. 3.2.4.1. Experimental Determination. The mixing enthalpies for the compositions (NaF/ThF_4) = (0.80:0.20), (0.70:0.30) were obtained at 1266 K (melting point of NaF) with DSC measurements. The measured mixing enthalpies (red circles) and the curve obtained from the CALPHAD model (red line) are shown in Figure 10. The mixing enthalpy values based on the quasi-chemical model of Beneš et al.[11] (dotted line, red) and the values of Mukherjee and Dash[36] (polynomial formalism, red circles) are indicated as well. The results are summarized in Table 4. It must be noted that neither assessment was developed using experimental mixing enthalpy data. Still, relatively good agreement was achieved between the experimental data obtained in this work and both models.

3.2.4.2. MD Calculations. The enthalpy was obtained directly from the mean of the internal energies calculated after the *NpT* run. The molar enthalpy was calculated for each temperature (1270, 1433, 1500, 1600, 1800, and 2000 K) over the full composition range (see Supporting Information). In

Table 4. Mixing Enthalpy in the NaF−ThF_4 System at 1266 ± 10 K and Standard Pressure (0.1 ± 0.01 MPa), as Determined in This Study

$x(ThF_4)$/mol %[a]	$\Delta_{mix}H$[b]/kJ mol^{-1}	m(NaF)[c]/mg	$m(ThF_4)$[c]/mg
19.9	−13.0 ± 1.1	7.5	13.7
30.2	−17.9 ± 0.9	7.1	22.5

[a]Standard uncertainty $u(x(ThF_4))$ = 0.5 mol %. [b]Error is based on the standard uncertainty determined during the calibration process. [c]Standard uncertainty $u(m)$ = 0.1 mg.

Figure 10, the results of the MD simulations at 1270 K are compared to the curve at 1266 K obtained from the CALPHAD optimization in our coupled model and to the experimental data. Similarly, the results of MD simulations at 1400 K (the potential parameters for the Li^+−Th^{4+}, Li^+−F^-, and Li^+−Li^+ interactions were taken from the study of Dewan et al.[15] (more details can be found in the Supporting Information), and the experimental data and CALPHAD optimization at 1121 K reported by Capelli et al.[40] for the LiF−ThF_4 system are shown. In both systems, the results obtained with MD are much more negative than the experimental data. An optimization of the phase diagram data with the CALPHAD method based on the MD mixing enthalpy values for the NaF−ThF_4 system at 1270 K was attempted. However, this was not successful, even when the thermodynamic data of the NaF−ThF_4 intermediates were adjusted substantially. Consequently, it is likely that the MD overestimates the mixing enthalpy data: a small difference between two large numbers is difficult to be captured accurately. Nevertheless, the compositions of the minima are similar, which are reached at 30 and 40 mol % ThF_4 for the MD and CALPHAD curve, respectively. The minima of the mixing enthalpy curves calculated with MD in Figure 10 around 30 mol % ThF_4 moreover agree well with the maxima of the excess molar volume seen in Figure 1 and minima of the average coordination number in Figure 4, which are situated around 30−40 mol % too: the region is characterized by complexes in which the fluorides are tightly bound to Th^{4+} and excess volume is found in the interstices between complexes. In

https://doi.org/10.1021/acs.jpcb.1c04830
J. Phys. Chem. B 2021, 125, 8558−8571

the phase diagram, this high stability of the liquid related to maximum short-range ordering is reflected in the relatively low melting point of Na_2ThF_6 (Figure 12).

3.2.5. Heat Capacities. The heat capacity was derived from the molar enthalpies calculated in steps of 10 mol % ThF_4 at 1433, 1500, 1600, 1800, and 2000 K. The heat capacities calculated from MD are shown in Figure 11. The calculated heat capacity with MD for ThF_4 is 170.7 J K^{-1} mol^{-1}, which agrees very well with the literature value of 168.0 ± 10 J K^{-1} mol^{-1}.[46] The calculated heat capacity of NaF was 68.1 J K^{-1} mol^{-1}, which differs slightly from the reported value of 73.0 J K^{-1} mol^{-1} (uncertainty not reported).[45]

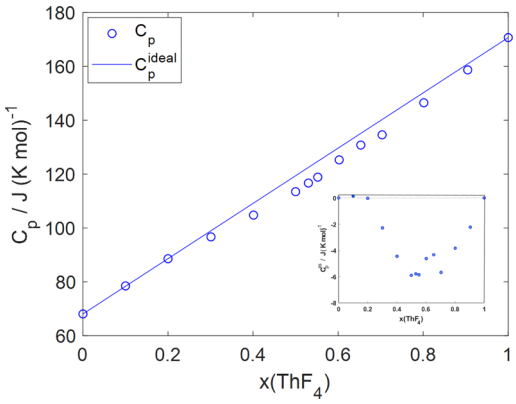

Figure 11. Evolution of heat capacity and ideal heat capacity in the NaF−ThF_4 system calculated from enthalpies obtained in MD simulations in the temperature region 1433−2000 K. Inset: excess heat capacity.

A slight negative deviation from ideal behavior is predominant across all compositions, with a maximum deviation of 5% at X_{ThF_4} = 0.5. This stands in contrast with the positive excess heat capacity in binary mixtures of lithium fluoride with other alkali fluorides, found by Beilmann et al. via drop calorimetry.[72] Beilmann et al. pointed out that an excess molar volume had been observed by Holm[73] in the same systems. Moreover, they suggested that both phenomena could be explained by the long-lived structures observed by Dracopolous and Papatheodorou[74] with Raman spectroscopy of the type $(LiF_x)A$ (A = K, Cs). On the one hand, the complexes could account for additional vibrational mechanisms for the storage of energy, explaining the increased heat capacity. On the other hand, if these complexes disturbed the close packing arrangement of the ions in the pure salts, then the excess volume would be accounted for. In the case of molten ThF_4, there are already chains present which contribute to the storing of energy: their partial disruption by the addition of Na^+ ions can explain a reduced capacity to retain heat with respect to the pure end member. The partial disruption of the network may also explain the positive excess volume in the NaF−ThF_4 case (Figure 1): similar to the disruption of loosely associated closely packed ions in the mixed alkali fluorides, a disruption of closely packed $[ThF_x]^{4-x}$ shells occurs, expanding the structure. The negative excess heat capacity is consistent with the negative excess thermal expansion (see Supporting Information), indicating a lower vibrational contribution to the total free energy than in an ideal mixture. Note that the ratio $C_P^{xs}/C_P = -0.052$ is close to $\beta^{xs}/\beta = -0.096$ as both thermal expansion and heat capacity originate from the vibrational state of the mixture.

3.3. Coupled Structural Thermodynamic Model of the NaF−ThF_4 System. The NaF−ThF_4 binary system

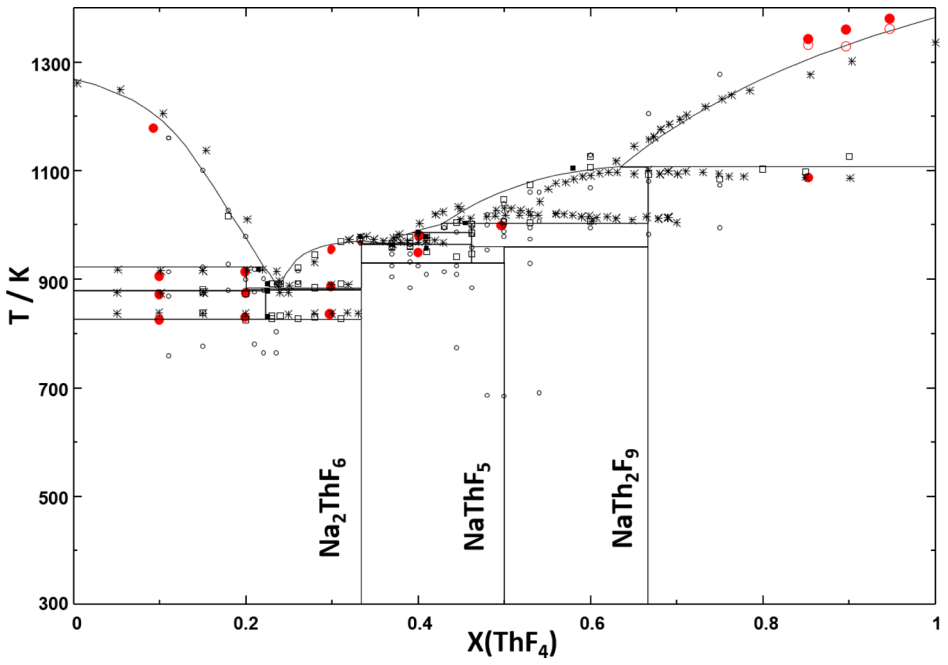

Figure 12. NaF−ThF_4 phase diagram as calculated in this work with the coupled structural thermodynamic model, compared to experimental data. The thermodynamic events measured in this work are indicated with red ●. The filled red circles near the liquidus in the 85−95 mol % region indicate the extremum temperature, and the hollow circles represent the onset temperature of the melting event. The phase diagram data reported by Emelyanov and Evstyukhin[51] are shown as *. The thermodynamic events obtained by Thoma et al.[50] are indicated with the remaining black symbols. Thermal analysis data are indicated with ○, quenching data with □, and invariant equilibria with ●.

https://doi.org/10.1021/acs.jpcb.1c04830
J. Phys. Chem. B 2021, 125, 8558−8571

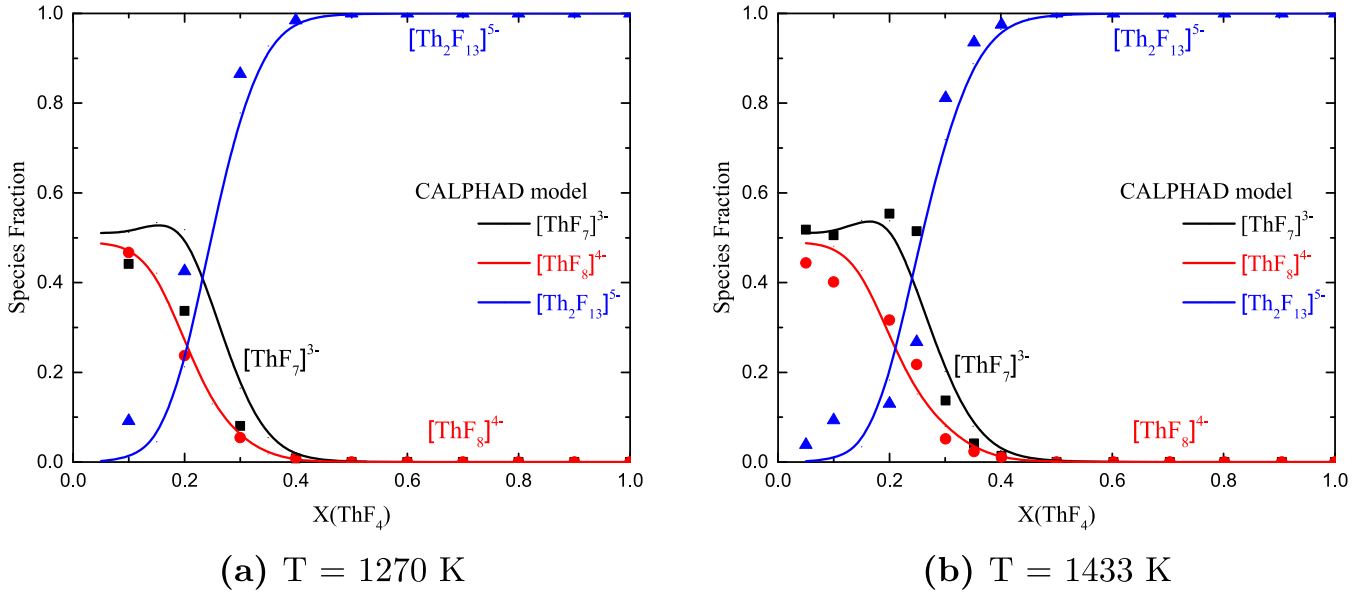

Figure 13. Complex anion distribution obtained with the CALPHAD model (solid lines) and compared with the MD data shown in Figure 5 (symbols): $[ThF_7]^{3-}$ (black), $[ThF_8]^{4-}$ (red), and $[Th_2F_{13}]^{5-}$ (blue). (a) T = 1270 K, (b) T = 1433 K.

shown in Figure 12 was optimized taking into account coordination and speciation information derived from MD simulations (Section 3.1), heat capacity (Section 3.2.3), mixing enthalpy (Section 3.2.4) and calorimetric data from the literature and measured in this work by DSC (Table 2). Overall, the calculated phase diagram reproduces the data gathered in this work satisfactorily, as well as the data from Thoma et al.,[50] and to a lesser extent, data by Emelyanov and Evstyukhin.[51] Additionally, the distribution of the main species $[ThF_7]^{3-}$, $[ThF_8]^{4-}$, and $[Th_2F_{13}]^{5-}$ could be reproduced accurately, as shown in Figure 13a,b.

The model moreover seems to perform adequately for properties which were not taken into account for its optimization. Figure 14 compares the activities calculated at T = 1241 K to determinations from mass-spectrometric measurements by Sidorov et al.[75] The NaF activities are reproduced remarkably well. Although in the case of ThF_4 the agreement is not excellent, the model is capable of correctly predicting a significant negative deviation from ideality below $X(ThF_4)$ = 0.3. The trend beyond that point, up until $X(ThF_4)$ = 0.5, is a relatively large negative deviation, and it is also correctly predicted. A negative deviation from ideality is typical for electrolytes in concentrated regimes and is directly linked to a reduced availability of dissociated ions due to their incorporation into associated structures: this negative deviation is closely linked to the negative excess in the enthalpy of mixing (Figure 10). The activities and the mixing enthalpies are thus related to the microscopic structure and are indicative of the stability of complexes in mixtures. Macroscopically, the implication is that the binary mixtures have a lower vapor pressure than the individual end members, which is of course desirable since low vapor pressures are a design requirement of MSRs.

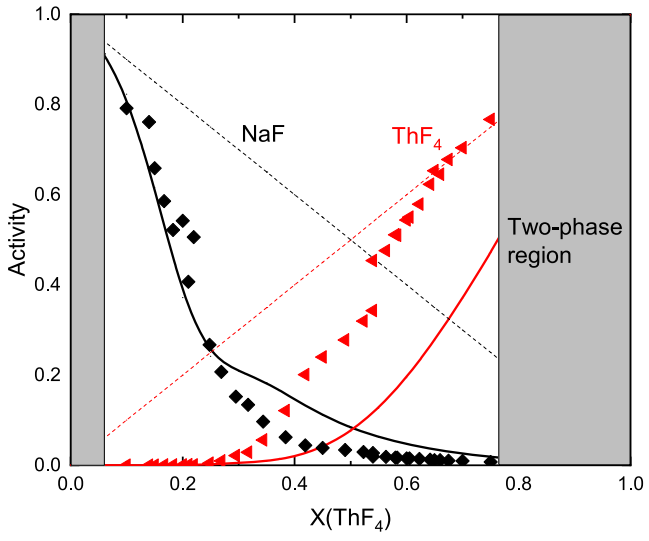

Figure 14. Activities in the $Na_xTh_{1-x}F_{4-3x}$ liquid solution at T = 1241 K. The solid lines correspond to the activities predicted by the present structural thermodynamic model. The symbols are experimental data by Sidorov et al.[75] at T = 1241 K. The dashed lines represent ideal behavior.

4. CONCLUSIONS

The thermodynamic, structural, and physicochemical properties of the NaF−ThF_4 system have been investigated with experimental and computational methods. The system is more complex than LiF−ThF_4, with more intermediate phases and larger deviations from ideality. Generally speaking, these deviations make NaF an adequate component in molten salt reactor fuels. Under neutron irradiation, an excess molar volume can be regarded as negative excess reactivity that is an inherent safety feature. The negative mixing enthalpy, related to the strong negative deviations in the activity, implies a reduced vapor pressure with respect to end members which themselves have a low vapor pressure, another beneficial feature. The negative excess heat capacity of the mixtures seems too small to be a concern; however, it deserves further study. Examining the transport properties, chiefly, the viscosity and thermal conductivity, is also needed.

https://doi.org/10.1021/acs.jpcb.1c04830
J. Phys. Chem. B 2021, 125, 8558−8571

■ ASSOCIATED CONTENT

Supporting Information

The Supporting Information is available free of charge at https://pubs.acs.org/doi/10.1021/acs.jpcb.1c04830.

Detailed descriptions of the potential used in the MD simulations, methodology of DFT and TSC calculations, CALPHAD modeling, DSC measurements, calculations of the density of the (Na,Th)F_x liquid solution, thermal expansions of the solid phases Na_2ThF_6, $NaTh_2F_9$, and thermal expansion and speciation of the liquid solution (PDF)

■ AUTHOR INFORMATION

Corresponding Author

Anna Louise Smith − *Faculty of Applied Sciences, Radiation Science & Technology Department, Delft University of Technology, 2629 JB Delft, The Netherlands;* orcid.org/0000-0002-0355-5859; Email: a.l.smith@tudelft.nl

Authors

Maarten B. J. W. Schreuder − *Faculty of Applied Sciences, Radiation Science & Technology Department, Delft University of Technology, 2629 JB Delft, The Netherlands*

Jaén A. Ocádiz Flores − *Faculty of Applied Sciences, Radiation Science & Technology Department, Delft University of Technology, 2629 JB Delft, The Netherlands;* orcid.org/0000-0002-9612-5478

Aimen E. Gheribi − *Centre for Research in Computational Thermochemistry, Department of Chemical Engineering, Ecole Polytechnique, Montreal H3C 3A7 Quebec, Canada;* orcid.org/0000-0002-5443-2277

Ondrej Beneš − *European Commission, Joint Research Centre (JRC), D-76125 Karlsruhe, Germany*

Jean-Christophe Griveau − *European Commission, Joint Research Centre (JRC), D-76125 Karlsruhe, Germany*

Eric Colineau − *European Commission, Joint Research Centre (JRC), D-76125 Karlsruhe, Germany*

Rudy J. M. Konings − *Faculty of Applied Sciences, Radiation Science & Technology Department, Delft University of Technology, 2629 JB Delft, The Netherlands; European Commission, Joint Research Centre (JRC), D-76125 Karlsruhe, Germany*

Complete contact information is available at: https://pubs.acs.org/10.1021/acs.jpcb.1c04830

Author Contributions

M.B.J.W.S.: conceptualization, methodology, investigation, formal analysis, visualization, data curation, writing−original draft preparation J.A.O.F.: conceptualization, methodology, supervision, investigation, formal analysis, visualization, data curation, writing−original draft preparation A.E.G.: conceptualization, investigation, software, formal analysis, visualization, writing−original draft preparation J.-C.G.: investigation E.C.: investigation O.B.: verification, resources R.J.M.K.: supervision, resources, writing−review & editing A.L.S.: conceptualization, methodology, supervision, funding acquisition, resources, project administration, writing−review & editing.

Notes

The authors declare no competing financial interest.

■ ACKNOWLEDGMENTS

The authors are grateful to Pavel Souček for providing us with ThF_4 of high purity. We would also like to thank Mathieu Salanne for the use of his MD code. A.L.S. acknowledges gratefully financial support from the Netherlands Organisation for Scientific Research (NWO) (project 722.016.005). J.A.O.F. would like to thank CONACYT-SENER for financial support.

■ REFERENCES

(1) Danek, V. *Physico-chemical Analysis of Molten Electrolytes*; Elsevier, 2006.

(2) Salanne, M.; Simon, C.; Turq, P. Heat-transport properties of molten fluorides: Determination from first-principles. *J. Fluorine Chem.* **2009**, *130*, 38−44.

(3) Salanne, M.; Simon, C.; Turq, P.; Heaton, R. J.; Madden, P. A. A first-principles description of liquid BeF_2 and its mixtures with LiF: 2. Network formation in LiF- BeF_2. *J. Phys. Chem. B* **2006**, *110*, 11461−11467.

(4) Fan, E.; Li, L.; Lin, J.; Wu, J.; Yang, J.; Wu, F.; Chen, R. Low-temperature molten-salt-assisted recovery of valuable metals from spent lithium-ion batteries. *ACS Sustainable Chem. Eng.* **2019**, *7*, 16144−16150.

(5) Siambun, N. J.; Mohamed, H.; Hu, D.; Jewell, D.; Beng, Y. K.; Chen, G. Z. Utilisation of carbon dioxide for electro-carburisation of mild steel in molten carbonate salts. *J. Electrochem. Soc.* **2011**, *158*, H1117.

(6) Weng, W.; Tang, L.; Xiao, W. Capture and electro-splitting of CO2 in molten salts. *J. Energy Chem.* **2019**, *28*, 128−143.

(7) Kamali, A. R. Clean production and utilisation of hydrogen in molten salts. *RSC Adv.* **2020**, *10*, 36020−36030.

(8) Murakami, T.; Nishikiori, T.; Nohira, T.; Ito, Y. Electrolytic synthesis of ammonia in molten salts under atmospheric pressure. *J. Am. Chem. Soc.* **2003**, *125*, 334−335.

(9) Beneš, O.; Konings, R. J. M. Molten Salt Reactor Fuel and Coolant. *Compr. Nucl. Mater.* **2012**, *3*, 359−389.

(10) Tosolin, A.; Souček, P.; Beneš, O.; Vigier, J.-F.; Luzzi, L.; Konings, R. J. M. Synthesis of plutonium trifluoride by hydro-fluorination and novel thermodynamic data for the PuF_3-LiF system. *J. Nucl. Mater.* **2018**, *503*, 171−177.

(11) Beneš, O.; Beilmann, M.; Konings, R. Thermodynamic assessment of the LiF-NaF-ThF_4-UF_4 system. *J. Nucl. Mater.* **2010**, *405*, 186−198.

(12) Madden, P. A.; Wilson, M. Covalent effects in ionic systems. *Chem. Soc. Rev.* **1996**, *25*, 339−350.

(13) Heaton, R. J.; Brookes, R.; Madden, P. A.; Salanne, M.; Simon, C.; Turq, P. A first-principles description of liquid BeF_2 and its mixtures with LiF: 1. Potential development and pure BeF_2. *J. Phys. Chem. B* **2006**, *110*, 11454−11460.

(14) Smith, A. L.; Verleg, M. N.; Vlieland, J.; de Haas, D.; Ocadiz-Flores, J. A.; Martin, P.; Rothe, J.; Dardenne, K.; Salanne, M.; Gheribi, A. E.; et al. In situ high-temperature EXAFS measurements on radioactive and air-sensitive molten salt materials. *J. Synchrotron Radiat.* **2019**, *26*, 124−136.

(15) Dewan, L. C.; Simon, C.; Madden, P. A.; Hobbs, L. W.; Salanne, M. Molecular dynamics simulation of the thermodynamic and transport properties of the molten salt fast reactor fuel LiF−ThF_4. *J. Nucl. Mater.* **2013**, *434*, 322−327.

(16) Gheribi, A. E.; Corradini, D.; Dewan, L.; Chartrand, P.; Simon, C.; Madden, P. A.; Salanne, M. Prediction of the thermophysical properties of molten salt fast reactor fuel from first-principles. *Mol. Phys.* **2014**, *112*, 1305−1312.

(17) Kresse, G.; Hafner, J. Ab initio molecular dynamics of liquid metals. *Phys. Rev. B: Condens. Matter* **1993**, *47*, 558−561.

(18) Kresse, G.; Hafner, J. Ab initio molecular-dynamics simulation of the liquid-metal-amorphous-semiconductor transition in germanium. *Phys. Rev. B: Condens. Matter* **1994**, *49*, 14251−14269.

(19) Kresse, G.; Furthmüller, J. Efficiency of ab-initio total energy calculations for metals and semiconductors using a plane-wave basis set. *Comput. Mater. Sci.* **1996**, *6*, 15−50.
(20) Kresse, G.; Furthmüller, J. Efficient iterative schemes for ab initio total-energy calculations using a plane-wave basis set. *Phys. Rev. B: Condens. Matter* **1996**, *54*, 11169−11186.
(21) Blöchl, P. E. Projector augmented-wave method. *Phys. Rev. B: Condens. Matter* **1994**, *50*, 17953−17979.
(22) Kresse, G.; Joubert, D. From ultrasoft pseudopotentials to the projector augmented-wave method. *Phys. Rev. B: Condens. Matter Mater. Phys.* **1999**, *59*, 1758−1775.
(23) Perdew, J. P.; Burke, K.; Ernzerhof, M. Generalized gradient approximation made simple. *Phys. Rev. Lett.* **1996**, *77*, 3865−3868.
(24) Perdew, J. P.; Burke, K.; Ernzerhof, M. Generalized Gradient Approximation Made Simple [Phys. Rev. Lett. 77, 3865 (1996)]. *Phys. Rev. Lett.* **1997**, *78*, 1396.
(25) Souček, P.; Beneš, O.; Claux, B.; Capelli, E.; Ougier, M.; Tyrpekl, V.; Vigier, J.; Konings, R. Synthesis of UF_4 and ThF_4 by HF gas fluorination and re-determination of the UF_4 melting point. *J. Fluorine Chem.* **2017**, *200*, 33−40.
(26) van der Meer, J. P. M.; Konings, R. J. M. Thermal and physical properties of molten fluorides for nuclear applications. *J. Nucl. Mater.* **2007**, *360*, 16−24 Proceedings has been selected.
(27) Le Bail, A.; Duroy, H.; Fourquet, J. L. Ab-initio structure determination of $LiSbWO_6$ by X-ray powder diffraction. *Mater. Res. Bull.* **1988**, *23*, 447−452.
(28) Rodriguez-Carvajal, J. *FULLPROF Program: Rietveld Pattern Matching Analysis of Powder Patterns*; Institut Laue-Langevin: Grenoble, 1990.
(29) Lashley, J. C.; Hundley, M. F.; Migliori, A.; Sarrao, J. L.; Pagliuso, P. G.; Darling, T. W.; Jaime, M.; Cooley, J. C.; Hults, W. L.; Morales, L.; et al. Critical examination of heat capacity measurements made on a Quantum Design physical property measurement system. *Cryogenics* **2003**, *43*, 369−378.
(30) Smith, A. L.; Pignié, M.-C.; van Eijck, L.; Griveau, J.-C.; Colineau, E.; Konings, R. J. M. Thermodynamic study of Cs3Na(MoO4)2: Determination of the standard enthalpy of formation and standard entropy at 298.15 K. *J. Chem. Therm.* **2018**, *120*, 205−216.
(31) Javorský, P.; Wastin, F.; Colineau, E.; Rebizant, J.; Boulet, P.; Stewart, G. Low-temperature heat capacity measurements on encapsulated transuranium samples. *J. Nucl. Mater.* **2005**, *344*, 50−55.
(32) Seifitokaldani, A.; Gheribi, A. E. Thermodynamically self-consistent method to predict thermophysical properties of ionic oxides. *Comput. Mater. Sci.* **2015**, *108*, 17−26.
(33) Seifitokaldani, A.; Gheribi, A. E.; Dollé, M.; Chartrand, P. Thermophysical properties of titanium and vanadium nitrides: Thermodynamically self-consistent approach coupled with density functional theory. *J. Alloys Compd.* **2016**, *662*, 240−251.
(34) Gheribi, A. E.; Seifitokaldani, A.; Wu, P.; Chartrand, P. An ab initio method for the prediction of the lattice thermal transport properties of oxide systems: Case study of Li_2O and K_2O. *J. Appl. Phys.* **2015**, *118*, 145101.
(35) Beneš, O.; Konings, R. J. M.; Wurzer, S.; Sierig, M.; Dockendorf, A. A DSC study of the $NaNO_3$−KNO_3 system using an innovative encapsulation technique. *Thermochim. Acta* **2010**, *509*, 62−66.
(36) Mukherjee, S.; Dash, S. Thermodynamic investigation of NaF-ThF_4 system and fuel salts of Molten Salt Reactor. *J. Fluorine Chem.* **2018**, *212*, 17−25.
(37) Höhne, G. W. H.; Cammenga, H. K.; Eysel, W.; Gmelin, E.; Hemminger, W. The temperature calibration of scanning calorimeters. *Thermochim. Acta* **1990**, *160*, 1−12.
(38) Cammenga, H. K.; Eysel, W.; Gmelin, E.; Hemminger, W.; Höhne, G. W. H.; Sarge, S. M. The temperature calibration of scanning calorimeters: Part 2. Calibration substances. *Thermochim. Acta* **1993**, *219*, 333−342.
(39) Boettinger, W. J.; Kattner, U. R.; Moon, K.-W.; Perepezko, J. H. *Methods for Phase Diagram Determination*; Zhao, J.-C., Ed.; Elsevier Science Ltd: Oxford, 2007, pp 151−221.
(40) Capelli, E.; Beneš, O.; Beilmann, M.; Konings, R. J. M. Thermodynamic investigation of the LiF−ThF_4 system. *J. Chem. Therm.* **2013**, *58*, 110−116.
(41) Ansara, I.; Sundman, B. *The Scientific Group Thermodata Europe in Computer Handling and Dissemination of Data*; Elsevier Science Publishers: Amsterdam, The Netherlands, 1986.
(42) Ocádiz-Flores, J. A.; Carré, E.; Griveau, J.-C.; Colineau, E.; Capelli, E.; Souček, P.; Beneš, O.; Konings, R. J. M.; Smith, A. L. Thermodynamic assessment of the KF-ThF_4, LiF-KF-ThF_4 and NaF-KF-ThF_4 systems. *J. Chem. Therm.* **2020**, *145*, 106069.
(43) Bale, C. W.; Bélisle, E.; Chartrand, P.; Decterov, S. A.; Eriksson, G.; Gheribi, A. E.; Hack, K.; Jung, I.-H.; Kang, Y.-B.; Melançon, J.; et al. FactSage thermochemical software and databases, 2010−2016. *Calphad* **2016**, *54*, 35−53.
(44) Leitner, J.; Voňka, P.; Sedmidubský, D.; Svoboda, P. Application of Neumann−Kopp rule for the estimation of heat capacity of mixed oxides. *Thermochim. Acta* **2010**, *497*, 7−13.
(45) Chase, M. W., Jr. NIST-JANAF Thermochemical tables 4th edition. *J. Phys. Chem. Ref. Data* **1998**, *85*.
(46) Tosolin, A.; Capelli, E.; Konings, R.; Luzzi, L.; Beneš, O. Isobaric Heat Capacity of Solid and Liquid Thorium Tetrafluoride. *J. Chem. Eng. Data* **2019**, *64*, 3945−3950.
(47) Smith, A. L.; Capelli, E.; Konings, R. J. M.; Gheribi, A. E. A new approach for coupled modelling of the structural and thermo-physical properties of molten salts. Case of a polymeric liquid LiF-BeF2. *J. Mol. Liq.* **2020**, *299*, 112165.
(48) Dai, J.; Long, D.; Huai, P.; Li, Q. Molecular dynamics studies of the structure of pure molten ThF_4 and ThF_4-LiF-BeF_2 melts. *J. Mol. Liq.* **2015**, *211*, 747−753.
(49) Ocádiz-Flores, J. A.; Gheribi, A. E.; Vlieland, J.; De Haas, D.; Dardenne, K.; Rothe, J.; Konings, R. J. M.; Smith, A. L. Examination of the short-range structure of molten salts: ThF_4, UF_4, and related alkali actinide fluoride systems. *Phys. Chem. Chem. Phys.* **2021**, *23*, 11091−11103.
(50) Thoma, R. E.; Insley, H.; Landau, B. S.; Friedman, H. A.; Grimes, W. R. Phase Equilibria in the Fused Salt Systems LiF−$ThF_4$and NaF−TfF_4. *J. Phys. Chem.* **1959**, *63*, 1266−1274.
(51) Emelyanov, V.; Evstyukhin, A. An investigation of fused-salt systems based on thorium fluoride-II. *J. Nucl. Energy* **1957**, *5*, 108−114.
(52) Desyatnik, V. N.; Klimenkov, A. A.; Kurbatov, N. N.; Nechaev, A. I.; Raspopin, S. P.; Chervinskii, Y. F. Density and kinematic viscosity of NaF-ThF_4 and KF-ThF_4 melts. *Sov. Atom. Energy* **1981**, *51*, 807−810.
(53) Kirshenbaum, A. D.; Cahill, J. A. The density of molten thorium and uranium tetrafluorides. *J. Inorg. Nucl. Chem.* **1961**, *19*, 65−68.
(54) Liu, J.-B.; Chen, X.; Qiu, Y.-H.; Xu, C.-F.; Schwarz, W. H. E.; Li, J. Theoretical Studies of Structure and Dynamics of Molten Salts: The LiF−ThF_4 System. *J. Phys. Chem. B* **2014**, *118*, 13954−13962.
(55) Toth, L. M.; Boyd, G. E. Raman spectra of thorium(IV) fluoride complex ions in fluoride melts. *J. Phys. Chem.* **1973**, *77*, 2654−2657.
(56) Adya, A. K.; Takagi, R.; Gaune-Escard, M. Unravelling the internal complexities of molten salts. *Z. Naturforsch.* **1998**, *53*, 1037−1048.
(57) Wilson, M.; Madden, P. A. "Prepeaks"and "first sharp diffraction peaks"in computer simulations of strong and fragile ionic liquids. *Phys. Rev. Lett.* **1994**, *72*, 3033.
(58) Pauvert, O.; Salanne, M.; Zanghi, D.; Simon, C.; Reguer, S.; Thiaudière, D.; Okamoto, Y.; Matsuura, H.; Bessada, C. Ion specific effects on the structure of molten AF-ZrF_4 systems (A^+= Li^+, Na^+, and K^+). *J. Phys. Chem. B* **2011**, *115*, 9160−9167.
(59) Zachariasen, W. H. Double Fluorides of Potassium or Sodium with Uranium, Thorium or Lanthanum. *J. Am. Chem. Soc.* **1948**, *70*, 2147−2151.
(60) Zachariasen, W. H. Crystal chemical studies of the 5f-series of elements. XII. New compounds representing known structure types. *Acta Crystallogr.* **1949**, *2*, 388−390.

https://doi.org/10.1021/acs.jpcb.1c04830
J. Phys. Chem. B 2021, 125, 8558−8571

(61) Zachariasen, W. H. Crystal chemical studies of the 5f-series of elements. I. New structure types. *Acta Crystallogr.* **1948**, *1*, 265−268.
(62) Thoma, R. E.; Insley, H.; Hebert, G. M.; Friedman, H. A.; Weaver, C. F. Phase Equilibria in the System NaF-ThF_4-UF_4. *J. Am. Ceram. Soc.* **1963**, *46*, 37−42.
(63) Grzechnik, A.; Fechtelkord, M.; Morgenroth, W.; Posse, J. M.; Friese, K. Crystal structure and stability of β-Na_2ThF_6 at non-ambient conditions. *J. Phys.: Condens. Matter* **2007**, *19*, 266219.
(64) Grzechnik, A.; Morgenroth, W.; Friese, K. Twinned tetragonal structure and equation of state of $NaTh_2F_9$. *J. Solid State Chem.* **2008**, *181*, 971−975.
(65) Underwood, C. C.; McMillen, C. D.; Kolis, J. W. The crystal structures of $CsTh_6F_{25}$ and $NaTh_3F_{13}$. *J. Chem. Crystallogr.* **2012**, *42*, 606−610.
(66) Le Bail, A. Whole powder pattern decomposition methods and applications: A retrospection. *Powder Diffr.* **2005**, *20*, 316−326.
(67) Blanco, M. A.; Francisco, E.; Luaña, V. GIBBS: isothermal-isobaric thermodynamics of solids from energy curves using a quasi-harmonic Debye model. *Comput. Phys. Commun.* **2004**, *158*, 57−72.
(68) Glensk, A.; Grabowski, B.; Hickel, T.; Neugebauer, J. Understanding Anharmonicity in fcc Materials: From its Origin to ab initio Strategies beyond the Quasiharmonic Approximation. *Phys. Rev. Lett.* **2015**, *114*, 195901.
(69) Grimvall, G. *Thermophysical Properties of Materials*; Elsevier, 1999.
(70) Mukherjee, S.; Dash, S. Determination of Gibbs energy of formation of $LiThF_5$, $LiTh_2F_9$, and $LiTh_4F_{17}$ in Li-Th-F system by using solid electrolyte galvanic cell. *J. Solid State Electrochem.* **2019**, *23*, 3043−3056.
(71) Barron, T.; White, G. K. *Heat Capacity and Thermal Expansion at Low Temperatures*; Springer Science & Business Media, 2012.
(72) Beilmann, M.; Beneš, O.; Capelli, E.; Reuscher, V.; Konings, R. J. M.; Fanghänel, T. Excess heat capacity in liquid binary alkali-fluoride mixtures. *Inorg. Chem.* **2013**, *52*, 2404−2411.
(73) Holm, J. L.; Kullberg, L.; Roti, I. Excess Volumes of Mixing in Liquid Binary Alkali-Halide Mixtures. *Acta Chem. Scand.* **1971**, *25*, 3609.
(74) Dracopoulos, V.; Papatheodorou, G. N. Isotropic and anisotropic Raman scattering from molten alkali-metal fluorides. *Phys. Chem. Chem. Phys.* **2000**, *2*, 2021−2025.
(75) Sidorov, L. N.; Zhuravleva, L. V.; Varkov, M. V.; Skokan, E. V.; Sorokin, I. D.; Korenev, Y. M.; Akishin, P. A. Mass-spectrometric determination of enthalpies of dissociation of gaseous complex fluorides into neutral and charged particles. VII. MF-ThF_4 systems (M= Li, Na, K, Rb, Cs). *Int. J. Mass Spectrom. Ion Phys.* **1983**, *51*, 291−311.

https://doi.org/10.1021/acs.jpcb.1c04830
J. Phys. Chem. B 2021, 125, 8558−8571